COMPOSITES SCIENCE AND TECHNOLOGY, Vol. 96, 23 May 2014, Pages 13–22.
DOI: http://dx.doi.org/10.1016/j.compscitech.2014.03.001 "

Numerical investigation of the impact behaviour of bioinspired nacre-like aluminium composite plates

E.A. Flores-Johnson[1,*], Luming Shen[1], Irene Guiamatsia[1], Giang D. Nguyen[2]

[1]School of Civil Engineering, The University of Sydney, Sydney, NSW 2006, Australia
[2]School of Civil, Environmental and Mining Engineering, University of Adelaide, Adelaide, SA 5005, Australia

Abstract: Inspired by the hierarchical structure of nacre, an aluminium alloy (AA) 7075 based composite featuring layer waviness and cohesive interface is studied as a low weight impact resistant material. To investigate the mechanical response and the ballistic performance of this laminated structure, a numerical study of the proposed nacre-like composite plates made of 1.1-mm thick AA 7075 tablets bonded with toughened epoxy resin was performed using Abaqus/Explicit. Target thicknesses of 5.4-mm, 7.5-mm and 9.6-mm impacted by a rigid hemi-spherical projectile were simulated. The epoxy material was modelled using a user-defined interface cohesive element with compressive strength enhancement. A significant performance improvement was recorded for the 5.4-mm nacre-like plate (compared to the same thickness bulk plate), which was explained by the hierarchical structure facilitating both localized energy absorption (by deformation of the tablet) and more globalized energy absorption (by inter-layered delamination and friction). For a given projectile, however, the performance improvement of using the proposed composite decreased with increasing laminate thickness, which was attributed to the increased likelihood of ductile failure occurring prior to perforation in thicker bulk plates. For 5.4-mm thick plates impacted at high velocity, the nacre-like plate had a better ballistic performance than that of the plates made of continuous (flat and wavy) layers, which was attributed to the larger area of plastic deformation (observed in the nacre-like plate after impact) due to the tablets arrangement.

Keywords: A. Layered structures; B. Impact behaviour.; B. Interface; C. Finite element analysis (FEA); Bioinspired composite.
[*]Corresponding author. Tel.: +61 2 9351 2113, Fax: +61 2 9351 3343, Email: emmanuel.flores-johnson@sydney.edu.au

1 INTRODUCTION

The demand for energy-absorbing lightweight engineering structures for blast and impact applications in automotive, aeronautical and defence industry is growing at a fast pace [1]. This trend poses a challenge for innovative engineering design to address the competing constraints of light weight on one hand, and impact and shock mitigation on the other hand. In this context, structural biological materials such as wood, bone and abalone shells, are an excellent source for inspiration [2] considering that evolutionary developments have resulted in high-performance lightweight composites structures, made of relatively weak and mundane constituents [3-5]. These biological materials deform via several high energy-absorbing mechanisms resulting in the improvement of structural and mechanical properties such as stiffness, strength and toughness.

Nacre, commonly known as the mother-of-pearl, is a biological material that exhibits outstanding mechanical properties due to its hierarchical structure that spans several scales [6]. It is a brick-wall patterned composite made of aragonite tablets (a brittle mineral), surrounded by

a soft organic biopolymer that "glues" them together [7]. Although nacre is made of 95% of aragonite, it exhibits a toughness of about 3000 times higher than that of aragonite [8]. This outstanding performance is attributed to the brick arrangement of the structure, the waviness of the tablets and the multiple interfaces between tablets [3, 9-11].

The performance of nacre-like engineering composites at the macroscale (millimetre-size) has only been scarcely explored [8, 10, 12, 13]; some recent investigations have shown their strong potential with respect to performance in sustaining impact and blast loading when compared to traditional laminated composite plates or bulk plates. A recent numerical work by Knipprath et al. [12] showed that the impact response of boron carbide ceramic can be improved by using a simplified nacre-like structural design that promotes crack delocalization. Tran et al. [14] also showed that nacre-like structural design can be used to improve the blast performance of glass fibre/thermoset resin composites.

The aim of this paper is to gain a better understanding of the mechanical behaviour of nacre-like aluminium composites under impact loading through a numerical parametric study of layered nacre-like plates made of 1.1-mm thick aluminium alloy (AA) 7075 tablets glued with toughened epoxy resin. The epoxy material was modelled using a user-defined cohesive element taking into account both the increase in strength and toughness when the debonding occurs under transverse interface compression, together with frictional effects after full debonding. Laminate thicknesses of 5.4-, 7.5- and 9.6-mm were modelled and the ballistic performance of bulk plates made of AA 7075 was compared with that of the equivalent (same thickness) nacre-like composites. For 5.4-mm thick plates impacted at high velocity, the ballistic performance of plates made of continuous (flat and wavy) layers was also studied. The problem description and validation of the numerical models are described in Section 2. Numerical results are presented and discussed in Section 3 followed by conclusions.

2 PROBLEM DESCRIPTION AND FINITE ELEMENT MODELLING

2.1 Problem description

To investigate the ballistic impact behaviour of nacre-like composite plates made of aluminium alloy with different thicknesses, the plates were impacted by a rigid 10-mm steel spherical projectile with a mass of 4.4 g and initial impact velocities in the range of 400-900 m/s. AA 7075-T651 was used for the target plates [15-17] (Table 1). A toughened epoxy adhesive Betamate 1044 was employed to model the interface between tablets and layers (Table 2). The parameters in Table 2 corresponding to the material properties of the epoxy resin used for the numerical model are identical to those required for standard cohesive elements (COH3D8) in Abaqus and were obtained from Wang et al. [18]. The two additional parameters in Table 2 used in the user-defined cohesive element, explained in Section 2.2.3, are the interface initial stiffness (in compression) K_s^f, which is taken to be two to three orders of magnitude less than interface initial stiffness (in tension) K_s (in this case *E*/interface thickness), as well as the coefficient of friction μ, which is assigned the rather common value of 0.2 [19].

Table 1 Material properties and Johnson-Cook model parameters for aluminium alloy.

Material properties	AA7075-T651 [15-17]
Density ρ (kg/m^3)	2700
Young's modulus E (GPa)	70
Poisson's ratio ν	0.3
Inelastic heat fraction η	0.9
Specific heat C_p (J/kgK)	910
Strain hardening	
A (MPa)	520
B (MPa)	477
n	0.52
Strain rate hardening	
Reference strain rate $\dot{\varepsilon}_0$ (s^{-1})	5x10^{-4}
C	0.001
Temperature softening	
Reference temperature T_r (K)	293
Melting temperature T_m (K)	893
m	1
Damage parameters	
D_1	0.096
D_2	0.049
D_3	-3.465
D_4	0.016
D_5	1.099
u_{pl}^f (mm)	0.0009

Table 2 Material properties and UEL parameters for epoxy resin.

Material properties	Betamate 1044 [18]
Density ρ (kg/m^3)	1350
Elastic modulus in the normal direction E (GPa)	3.1
Elastic modulus in the transverse directions G_1, G_2 (GPa)	1.55
Maximum normal traction t_n (MPa)	85.5
Maximum shear traction t_s (MPa)	70
Critical energy-release rate mode I G_{Ic} (J/m^2)	1680
Critical energy-release rate mode II G_{IIc} (J/m^2)	3570
UEL parameters	
Mohr-Coulomb coefficient of friction μ	0.2
Compressive shear stiffness K_s^f (MPa/0.05 mm)	3.1

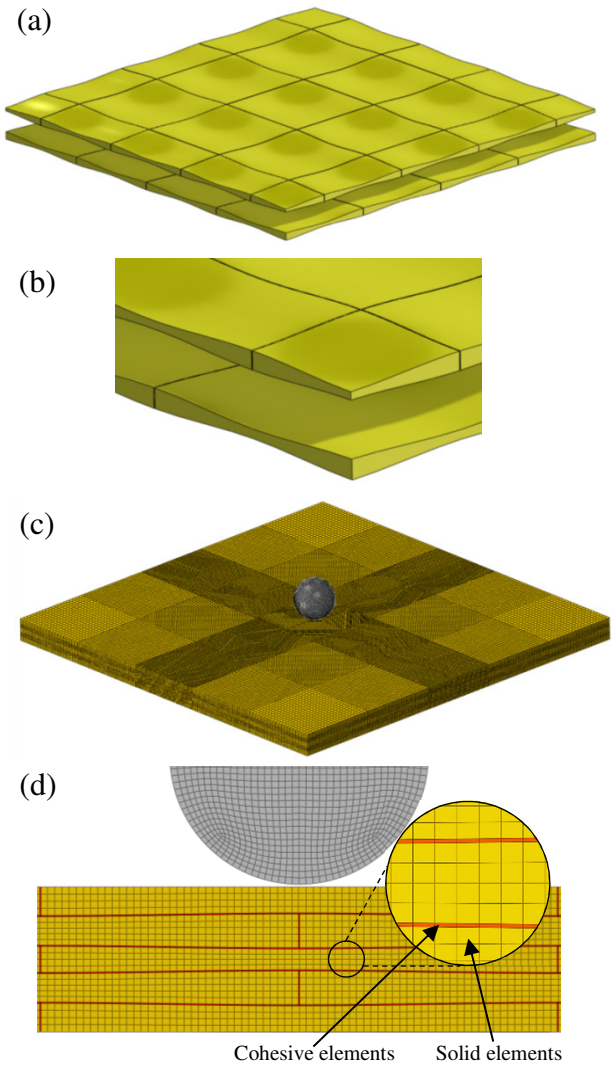

Fig. 1 (a) Solid geometry of individual layers, (b) closed-up view of individual layers, (c) finite-element mesh of 5-layer plate, (d) Mesh cross-section of the model.

The solid geometry of the 3D full model, inspired by the structure of nacre, consisted of a 100 mm × 100 mm plate made with aluminium alternate layers of 1.2-mm and 0.9-mm thick AA 7075 (Fig. 1). Targets of 5, 7 or 9 layers with total thicknesses of 5.4-, 7.5- or 9.6-mm, respectively, were simulated. Each layer, made of twenty-five 20 mm × 20 mm square tablets, was displaced with respect to its adjacent upper or/and lower neighbouring layer in such a way that individual tablets overlapped 1/4 of the surface area (Fig. 1). This overlapping is sufficiently close to the 1/3 of the surface overlap observed in the natural nacre material [9]. The waviness of the tablets was generated using a sinusoidal function with a wavelength of 20 mm and amplitude of 0.1 mm (Fig. 1). The solid geometry was generated using the computer-aided design software SolidWorks 2012 (Dassault Systemes, SolidWorks Corp., France) and then imported into Abaqus/Explicit (Version 6.11) [20] for pre- and post-processing.

The mesh comprised of reduced-integration linear hexahedral elements (C3D8R) for the solid tablets and the rigid projectile, as well as user-defined elements (UEL, described in Section 2.2.3) for the cohesive interface between tablets and bondline. These interface elements are 0.05-mm thick and have coincident nodes with the adjacent solid elements. Although Abaqus/Explicit allows zero-thickness geometry in cohesive elements, it still requires a nominal thickness to calculate the initial elastic stiffness and density. This thickness can either be specified directly as an input to the constitutive model while the geometric model has zero-thickness interface elements, or used to geometrically model the cohesive elements as a finite-thickness layer. The latter approach was adopted in this investigation because it made the task of model generation significantly easier. The in-plane mesh was skewed to be finer towards the impact region (centre of the plate) with an average element size of 0.27×0.27×0.27 mm^3

as illustrated in Fig. 1. The target plates were fully clamped at all of the edge boundaries. The number of elements for each solid layer and cohesive interface layer were 135360 and 3240, respectively, and a mesh sensitivity analysis presented in Section 2.4 confirms that this level of refinement was sufficient to obtain a converged solution. The automatic time incrementation scheme available in Abaqus/Explicit was employed. This scheme ensures that a stable time increment, based on the time required to propagate a dilatational wave across the smallest element in the model, is used. The estimated time is conservative, which will give a smaller time increment than the true limit that is based upon the maximum frequency of the entire model. The simulation time for the 9.6-mm thick nacre-like plate, using a 16-CPU high performance computer with 42 gigabytes of RAM, was seven hours for an initial impact velocity of 400 m/s.

2.2 Material models

The Johnson-Cook material model [21] was used together with the Johnson-Cook fracture criterion [22] to simulate the constitutive response of the solid tablets, while a user-defined cohesive element with compression-enhanced traction separation law [19] was used for the cohesive interface layer between the tablets. An overview of each model is provided herein for the sake of completeness.

2.2.1 Johnson-Cook constitutive model

The Johnson-Cook (JC) constitutive model [21] is an empirical model, where the equivalent stress σ_{eq} is given as a function of an equivalent plastic strain ε_{eq}, dimensionless plastic strain rate $\dot{\varepsilon}^*_{eq} = \dot{\varepsilon}_{eq}/\dot{\varepsilon}_0$ and temperature, as follows:

$$\sigma_{eq} = (A + B\varepsilon_{eq}^n)(1 + C\ln\dot{\varepsilon}^*_{eq})(1 - T^{*m}), \quad (1)$$

In the above, A, B, n, C and m are material constants and the homologous temperature T^* is defined as $T^* = (T - T_r)/(T_m - T_r)$, where T is the absolute temperature, T_r is the room temperature and T_m is the melting temperature; $\dot{\varepsilon}_{eq}$ and $\dot{\varepsilon}_0$ are the equivalent plastic strain rate and a user-defined strain rate, respectively.

During transient plastic deformation (which would normally occur under ballistic impact), material softening may occur due to localised adiabatic heating [23, 24]. Abaqus/Explicit allows to include these effects by computing the increase in the heat flux per unit volume r_{pl},

$$r_{pl} = \eta\boldsymbol{\sigma} : \dot{\boldsymbol{\varepsilon}}_{pl}, \quad (2)$$

where η is the inelastic heat fraction, $\boldsymbol{\sigma}$ is the stress and $\dot{\boldsymbol{\varepsilon}}_{pl}$ is the plastic strain rate. The heat change per unit volume can be expressed as,

$$r_{pl} = \rho C_P \Delta\mathrm{T}, \quad (3)$$

where ρ is the material density, C_P is the specific heat and ΔT is the change in temperature. By substituting Eq. (3) in Eq. (2) and using an integral form, the rise in temperature due to adiabatic heating is expressed as:

$$\Delta\mathrm{T} = \int_0^{\varepsilon_{pl}} \frac{\eta\sigma d\varepsilon_{pl}}{\rho C_P}, \quad (4)$$

2.2.2 Johnson-Cook (JC) fracture criterion

The Johnson-Cook (JC) fracture criterion, based on damage accumulation at an element integration point, is defined as the ratio of the increment of the equivalent plastic strain $\Delta\varepsilon_{eq}$, during an integration cycle, to a threshold equivalent fracture strain ε_f^{JC} [22]:

$$D_{JC} = \sum \frac{\Delta\varepsilon_{eq}}{\varepsilon_f^{JC}}, \quad (5)$$

Here D_{JC} is the damage parameter and the equivalent fracture strain is given by:

$$\varepsilon_f^{JC} = (D_1 + D_2\exp(D_3\sigma^*))(1 + D_4\ln\dot{\varepsilon}^*_{eq})(1 + D_5T^*), \quad (6)$$

where D_1 ,…, D_5 are material constants and $\sigma^* = \sigma_m/\sigma_{eq}$ is the stress triaxiality where σ_m represents the hydrostatic stress. Material degradation starts when $D_{JC} = 1$. Once the damage initiation criterion has been reached,

the effective plastic displacement, u_{pl}, is defined with the following damage evolution equation [20]:

$$u_{pl} = L\varepsilon_{pl}, \quad (7)$$

where L is the characteristic length of the element and ε_{pl} is the plastic strain. For reduced-integration linear hexahedral elements, L is defined as the typical length of a line across the element [20]. Before damage initiation, $u_{pl} = 0$. If a linear evolution of the damage variable d with effective plastic displacement is assumed, the damage variable increases according to [20]:

$$d = \frac{u_{pl}}{u_{pl}^f}, \quad (8)$$

where u_{pl}^f is the effective plastic displacement at complete failure of the material defined by the user. When complete failure occurs $(d = 1)$, the failed element is removed from the model mesh.

2.2.3 User defined cohesive element formulation

The constitutive behaviour of the cohesive interface between tablets and layers is capable of capturing the coupled response among mixed-mode debonding, plasticity and friction, and is presented in detail elsewhere [19]. A brief description of only the damage/friction coupled model is provided here.

The derivation of the model follows the framework of coupled dissipative processes described in [25], where only two energy functions, the Helmholtz free energy Ψ and the dissipation potential Φ, are needed to derive the constitutive relations and the evolution equations. The proposed Helmholtz free energy is:

$$\Psi = (1-D)\left\{\frac{1}{2}K_n u_n^2 + \frac{1}{2}K_s u_s^2\right\} + [1-H(u_n)]D\left\{\frac{1}{2}K_n u_n^2 + \frac{1}{2}K_s^f (u_s - u_{sc})^2\right\}, \quad (9)$$

The internal variables associated with energy dissipation are the damage indicator D and the permanent shear deformation due to friction u_{sc}. This representation effectively corresponds to a decomposition of the interface into a pristine or integral part $(1-D)$ where damage dissipation takes place and a fully damaged or cracked part (D) where frictional dissipation occurs. In Eq. (9) above, the indices n and s correspond to the local normal and shear directions, respectively; u is the interface separation, K is the initial interface stiffness, with K_s^f $(K_s^f \ll K_s)$ being the shear stiffness of the fully damaged interface. The Heaviside function $H(.)$ is used to detect whether or not the interface is under transverse compression so as to trigger the frictional mechanism.

From the above expression of the free energy, the constitutive relation between traction (t) and separation (u) are derived:

$$t_n = \begin{cases} (1-D)K_n u_n, & \text{if } u_n > 0 \\ K_n u_n, & \text{if } u_n \le 0 \end{cases}, \quad (10)$$

$$t_s = \begin{cases} t_{si} = (1-D)K_s u_s, & \text{if } u_n > 0 \\ t_{si} + t_{sc} = (1-D)K_s u_s + DK_s^f (u_s - u_{sc}), & \text{if } u_n \le 0 \end{cases} \quad (11)$$

Note that the interface shear traction is the sum of the traction on the integral part (t_{si}) and the traction of the cracked part (t_{sc}). The energy driving the damage process is obtained by taking the derivative of the free energy with respect to the damage parameter:

$$\chi = -\frac{\partial \Psi}{\partial D} = \chi_n + \chi_{si} - \chi_{sc}, \quad (12)$$

where

$$\chi_n = \begin{cases} \frac{1}{2}K_n u_n^2, & \text{if } u_n > 0 \\ 0, & \text{if } u_n \le 0 \end{cases}, \chi_{si} = \frac{1}{2}K_s u_s^2,$$

$$\chi_{sc} = \begin{cases} 0, & \text{if } u_n > 0 \\ \frac{1}{2}K_s^f (u_s - u_s^f)^2, & \text{if } u_n \le 0 \end{cases}, \quad (13)$$

Following Einav et al. [25], the dissipation potential Φ is assumed as the quadratic norm of two functions, each of which is homogeneous and of first order in terms of the associated internal variable:

$$\Phi = \sqrt{{\varphi_D}^2 + {\varphi_s^f}^2} \quad , \tag{14}$$

$$\varphi_D = \frac{\chi}{\sqrt{\frac{\chi_n}{F(D)} + \frac{2\chi_{si}K_S(1-D)^2}{\left[(1-D)\sqrt{2F(D)K_S} + \mu\langle -t_n\rangle\right]^2}}}\delta D \ , \tag{15}$$

$$\varphi_s^f = [\mu\langle -t_n\rangle + X]\delta u_s^f \ , \text{ where,}$$

$$X = \sqrt{\frac{2F(D)D(1-D)^2K_SK_s^f}{2(1-D)K_S + DK_s^f}} \tag{16}$$

In the above, the damage function $F(D)$ is a function provided in [19] which controls the evolution of failure process.

The yield function written in mixed energy and stress space, together with the evolution equations are derived from the dissipation potential using the Legendre transformation as follows:

$$y^* = \left(\frac{\chi}{\frac{\partial \varphi_D}{\partial \delta D}}\right)^2 + \left(\frac{t_{sc}}{\frac{\partial \varphi_s^f}{\partial \delta u_s^f}}\right)^2 - 1 \le 0,$$

$$\delta D = \delta\lambda\frac{\partial y^*}{\partial \chi}, \qquad \partial u_s^f = \delta\lambda\frac{\partial y^*}{\partial t_{sc}}, \tag{17}$$

Substituting the expressions for the dissipation potentials in Eq. (17) gives the yield function in stress space, written here separately for the tensile and compressive mode for the sake of clarity and also illustrated in Fig. 2a:

$$y = \begin{cases} (+): \frac{\frac{1}{2(1-D)^2}\left(\frac{t_n^2}{K_n} + \frac{t_s^2}{K_S}\right)}{F(D)} - 1 = 0 \\ (-): \frac{t_{si}^2}{\left[(1-D)\sqrt{2F(D)K_S} + \mu\langle -t_n\rangle\right]^2} + \left(\frac{t_{sc}}{\mu\langle -t_n\rangle + X}\right)^2 - 1 = 0 \end{cases}, \tag{18}$$

In that figure, the yield surface at different damage level is plotted. The strength increase in compression is clearly seen, and the model behaves as a Mohr-Coulomb friction model once the interface is fully delaminated, indicated by D=1. This model was implemented as a user-defined interface element in Abaqus/Explicit and separately tested using a single interface element as shown in Fig. 2b. In this example, one face of the interface element is fully constrained while the other with assigned transverse and shear displacements so as to reproduce certain desired combinations of normal/shear tractions. In this case, the properties of the interface were as follows: Y_n = Y_s = 50MPa, G_{Ic} = 281N·m/m^2, G_{IIc} = 800N·m/m^2, K_n = K_s = 10^9Pa/2×10^{-5}m; K_s^f = 10^7Pa/2×10^{-5}m ; μ = 0.3. As expected, the strength (peak force) and toughness (area under the shear stress-shear displacement plot) of the interface both increase with increasing transverse compressive loads. Under combined transverse tension and shear loading, the peak shear stress is lower because the mixed-mode loading condition expectedly causes the damage to initiate and propagate earlier.

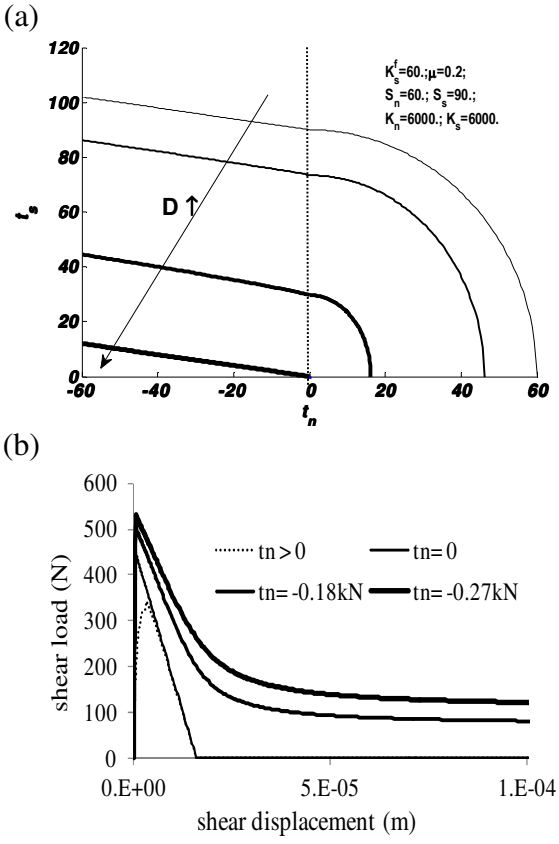

Fig. 2 (a) Evolution of the yield locus with the damage level; (b) shear load against shear displacement plots.

2.3 Validation of the JC material model and material parameters

The JC material model has been successfully employed to model ballistic impact on

aluminium plates [15, 24, 26-29] and the parameters used in our model are reported in Table 1 and were validated against independent experimental observations of aluminium plates. Materials parameters for JC material model in Table 1 were obtained from [15], while damage parameters for the JC fracture criterion were obtained from [16, 17].

Experimental results of the ballistic impact AA 7075-T651 plates reported by Børvik et al. [15] were used for model validation. In their experiments, target plates with dimension 600 mm × 600 mm and nominal thickness of 20 mm were clamped in a 500 mm diameter circular frame. The targets were impacted by a hardened steel 20-mm diameter projectile with a mass of 197 g using a compressed gas-gun for separate blunt and ogival nose shapes [15]. Numerical and experimental results are compared in Fig. 3. The solid lines in this figure are fits to the data of the Recht-Ipson model employed to predict the residual velocity V_r [30, 31],

$$V_r = a(V_i^P - V_{bl}^P)^{1/P}, \qquad (19)$$

where a and P are the empirical constants employed to best fit the data and V_{bl} is the ballistic limit. Good agreement between the empirical data and numerical results was observed in Fig. 3. An underestimation of 9.3% and an overestimation of 3.2% of the ballistic limits are observed for blunt and ogival projectiles, respectively (Figs. 3a, 3b).

Figures 3c and 3d show the predicted perforation process of Al 7075-T651 plates impacted by flat and ogival projectiles, respectively. It can be observed that some of the physical characteristics observed experimentally in the penetration process of Al 7075-T651 plates by Borvik et al. [15] were accurately captured by the numerical model; for instance, spalling and fragmentation on the plate back face.

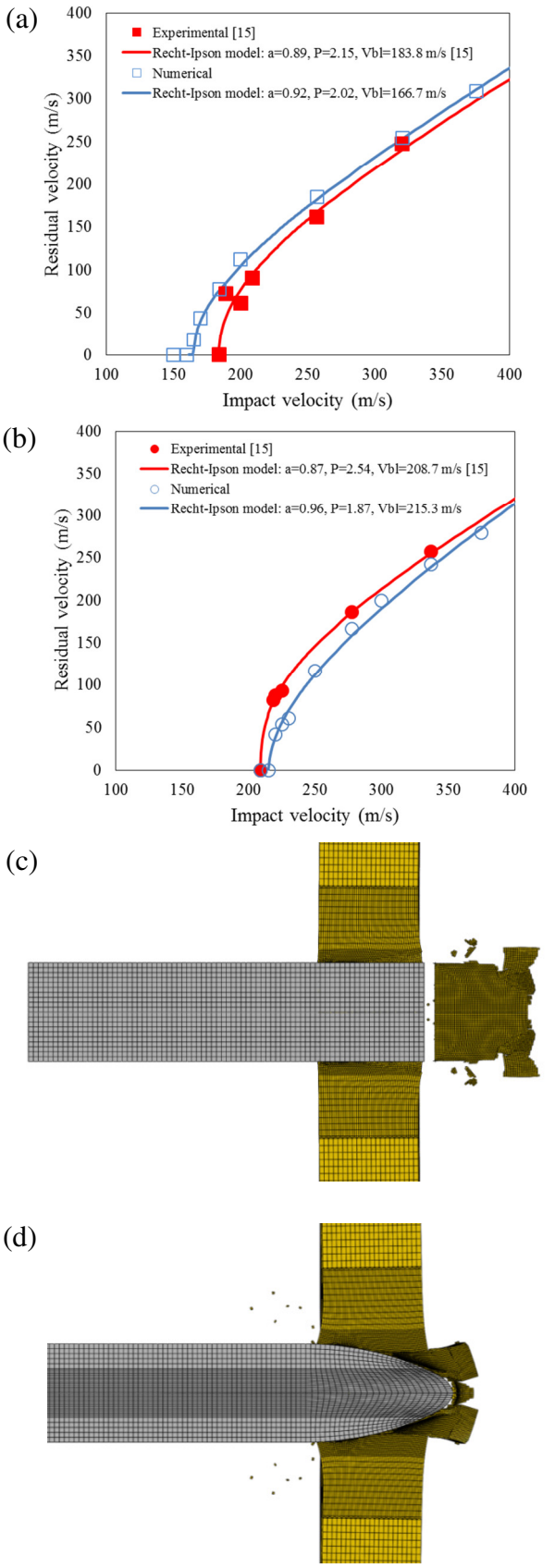

Fig. 3 Comparison between experimental [15] and predicted residual velocities for a 20-mm thick Al 7075-T651 plate impacted by (a) blunt projectile; (b) ogival projectile. Simulated perforation of the plate by (c) blunt projectile; (d) ogival projectile.

2.4 Mesh sensitivity analysis

A mesh sensitivity analysis was carried out for the simulations used to validate the model parameters of 20-mm thick plates of AA 7075-T651 impacted by 20-mm diameter blunt and ogival projectiles [15]. Six different element sizes were used in the impact region: 0.21×0.21×0.21 mm^3, 0.27×0.27×0.27 mm^3, 0.32×0.32×0.32 mm^3, 0.42×0.42×0.42 mm^3, 0.51×0.51×0.51 mm^3 and 1×1×1 mm^3 resulting in 96, 75, 63, 48, 39 and 20 through-thickness elements. Figure 4 shows the projectile residual velocity predicted using different numbers of through-thickness elements. The difference between the results with 96 and 63 through-thickness elements is less than 2%. Based on this analysis, a mesh size of 0.27×0.27×0.27 mm^3 was deemed sufficient for convergence and used throughout in this work to optimize the computational efficiency.

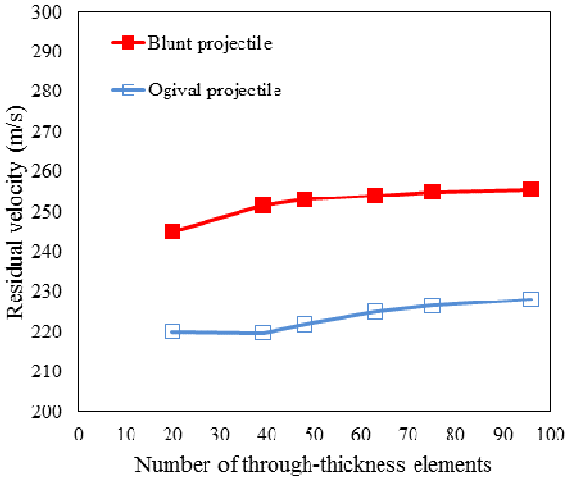

Fig. 4 Predicted projectile residual velocities using different numbers of through-thickness elements for 20-mm thick Al 7075-T651 plate impacted by blunt and ogival projectiles.

3 RESULTS AND DISCUSSION

3.1 Ballistic performance

To assess the ballistic performance of the different configurations, plots of residual velocity versus impact velocity are depicted in Figure 5. The solid lines represent fits to the numerical data of the Retch-Ipson model (Eq. (19)). For the 5.4-mm thick AA 7075 plate, it is very clear that the nacre-like structure performed better than the equivalent bulk plate, enabling a 10.2% reduction of the residual velocity and a 8.5% increase of the ballistic limit for an incident impact velocity of 900 m/s. The better performance of the 5.4-mm nacre-like composite is, as expected, due to the hierarchical material structure, which enables both localized energy absorption by deformation of the metallic tablet and semi-globalized energy dissipation in the interface debonding and friction, keeping in mind that the interaction surfaces here are further augmented because of the tablet waviness. As a result of the many dissipation mechanisms activated during the ballistic impact, the overall plastic deformation of the aluminium tablets also appears to be more distributed throughout the composite structure, as opposed to the bulk one (Fig. 6(a-b)). In comparison, the 5.4-mm bulk plate fails by brittle fracture and fragmentation (Fig. 6a) resulting in less energy absorption and a very localized area of plastic deformation (PEEQ) when compared to the larger area of plastic deformation observed in the nacre-like material (Fig. 6b). This brittle behaviour has been reported in other numerical simulations [28] and experimental results [15] of bulk plate of AA 7075.

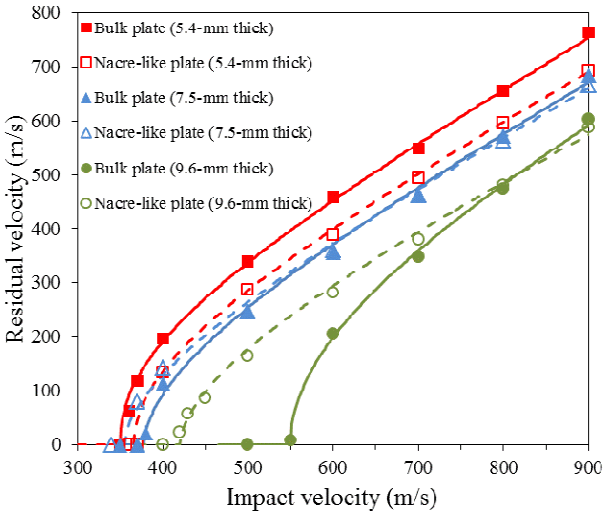

Fig. 5 Predicted projectile residual velocities versus impact velocity for bulk and nacre-like plates of 5.4-, 7.5- and 9.6-mm thicknesses.

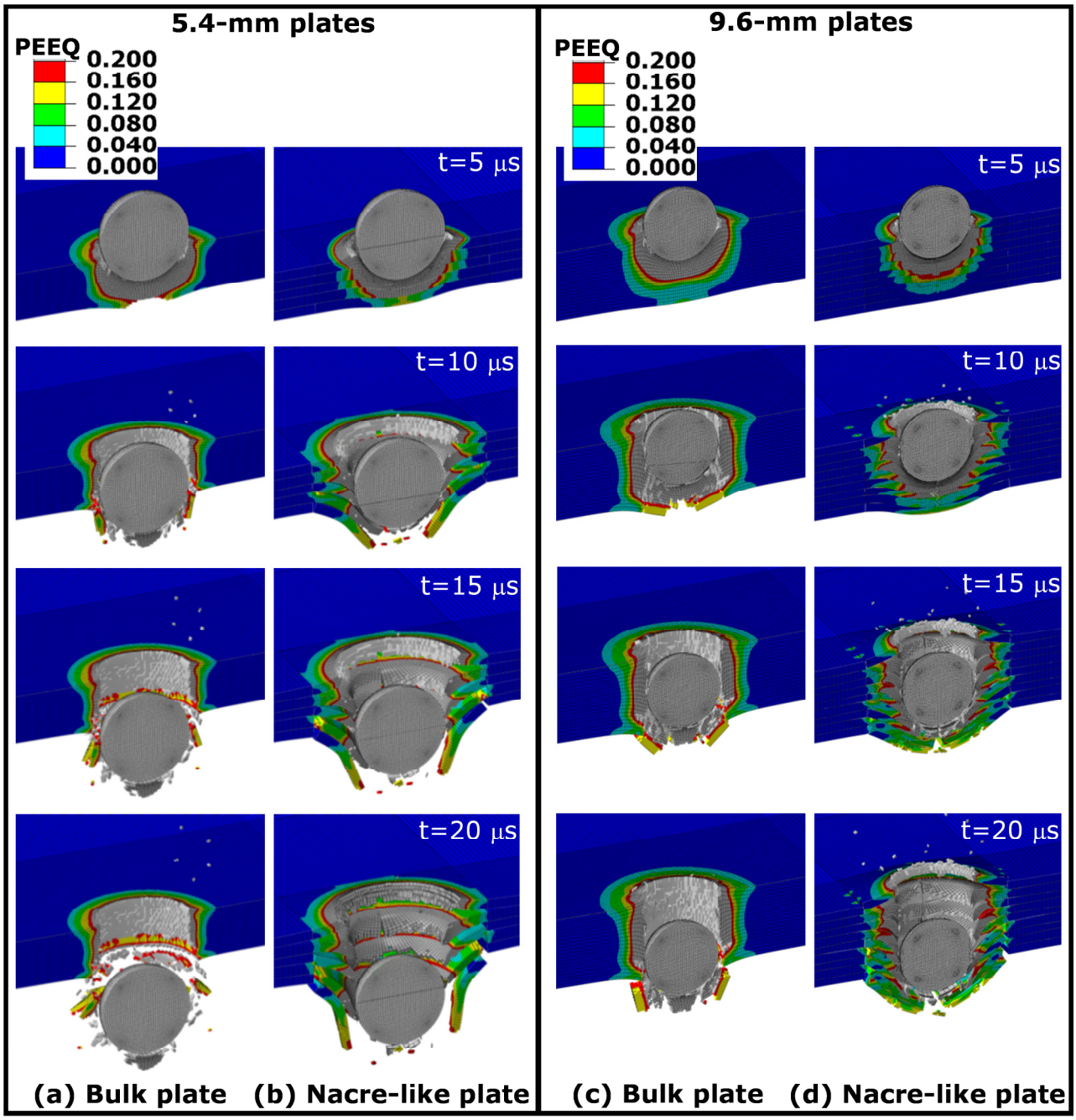

Fig. 6 Penetration process of Al 7075-T65 plates impacted by a 10-mm spherical projectile at 900 m/s: (a) 5.4-mm bulk plate; (b) 5.4-mm nacre-like plate; (c) 9.6-mm bulk plate; (d) 9.6-mm nacre-like plate.

It can be seen in Fig. 5 that for the 7.5-mm nacre-like plate, the reduction of the residual velocity is around 3% when compared to the bulk plate, while for the 9.6-mm nacre-like plate is less than 1% for an impact velocity of 900 m/s. This can also be explained by the previous argument: thicker bulk plates already exhibit significant ductile failure by hole enlargement before plugging and/or brittle failure is observed (Fig. 6c).

This behaviour leads to an increase of the bending resistance of thicker bulk plates, which already allows plastic deformation in a larger area. In these circumstances, the comparative advantage of the layered structure is therefore less significant.

Figure 5 also shows that the 7.5- and 9.6-mm thick nacre-like structures performed worse than the bulk plate for impact velocities lower than 600 m/s and 800 m/s, respectively.

This can be explained by the fact that the bending resistance of the bulk plates increased with the decrease of impact velocity.

Figure 7 shows the projectile velocity versus time curve for the 5.4-mm thick bulk and nacre-like plates impacted under an initial velocity of 900 m/s. Perforation of plates at $t = 0.004$ ms and 0.008 ms is also depicted. At $t = 0.004$ ms, the projectile velocity was $V \approx 800$ m/s for the bulk plate; and $V \approx 780$ m/s for the nacre-like plate. This difference is explained by the fact that there is a reduction of bending stiffness in the bulk plate due to the brittle failure in the back of the plate. This observation is more evident at $t = 0.008$ ms with $V \approx 770$ m/s for the bulk plate; and $V \approx 710$ m/s for the nacre-like plate. At this time, large fragmentations are observed in the bulk plate.

Figure 8 shows the damaged area in the four cohesive layers in the 5.4-mm nacre-like plate; the extent of debonding is predicted to be up to four projectile diameters.

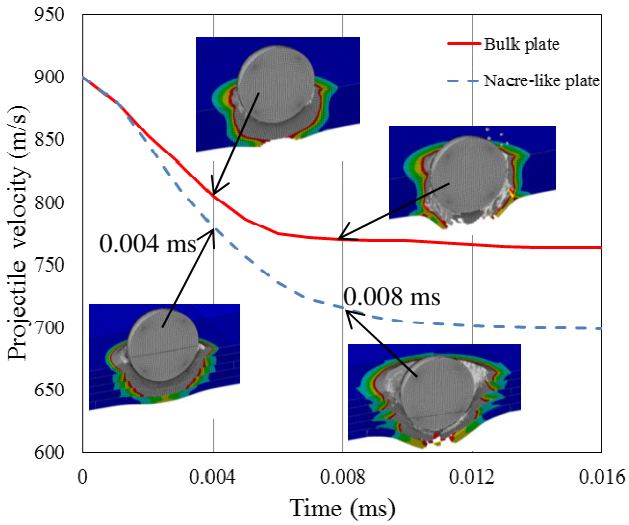

Fig. 7 Projectile velocity history of the penetration of 5.4-mm thick bulk and nacre-like plates for an initial impact velocity of 900 m/s.

3.2 Impact energy absorption

Figures 9(a)-(b) show the components of impact energy absorbed by the 5.4-mm bulk and nacre-like plates, respectively, for an impact velocity of 900 m/s. The kinetic energy of the projectile is mainly transformed into plate kinetic energy and dissipated through plastic deformation of the tablets, with the dissipation through debonding being much less significant. It can be seen that it is not the interface failure itself that causes the increased energy loss. Instead, such failure causes an in-plane load redistribution, thereby inducing a more diffuse plastic deformation of the tablets, which here is the dominant energy dissipation mechanism (Fig. 9). In addition, the energy loss attributed to frictional contact between fully delaminated tablets is significantly higher than the loss through friction in the failure of the bulk plate, despite a conservative value of μ=0.2, which was taken for the friction after full debonding. This frictional mechanism contributes to the dissipation of kinetic energy of the projectile and hence the reduction of its residual velocity at the end.

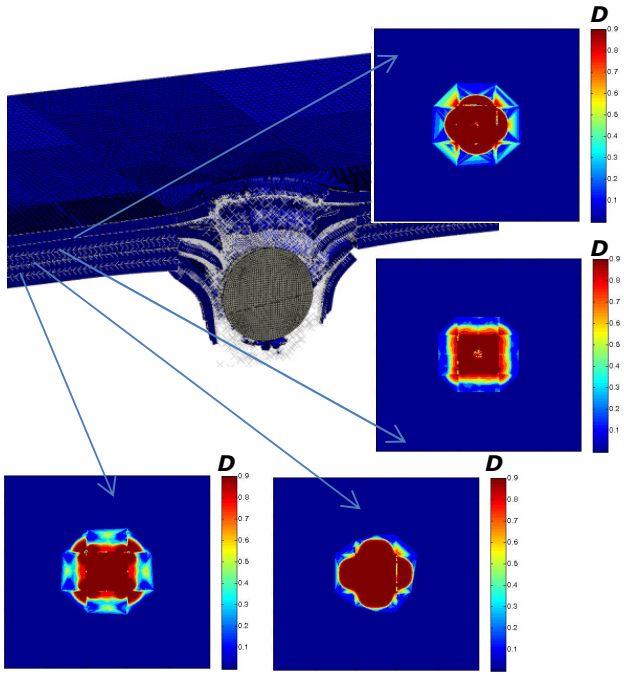

Fig. 8 Damage area of cohesive element layers (indicated by the damage parameter D of the constitutive model) of a 5.4-mm thick AA 7075 nacre-like plate impacted by a spherical projectile at 900 m/s.

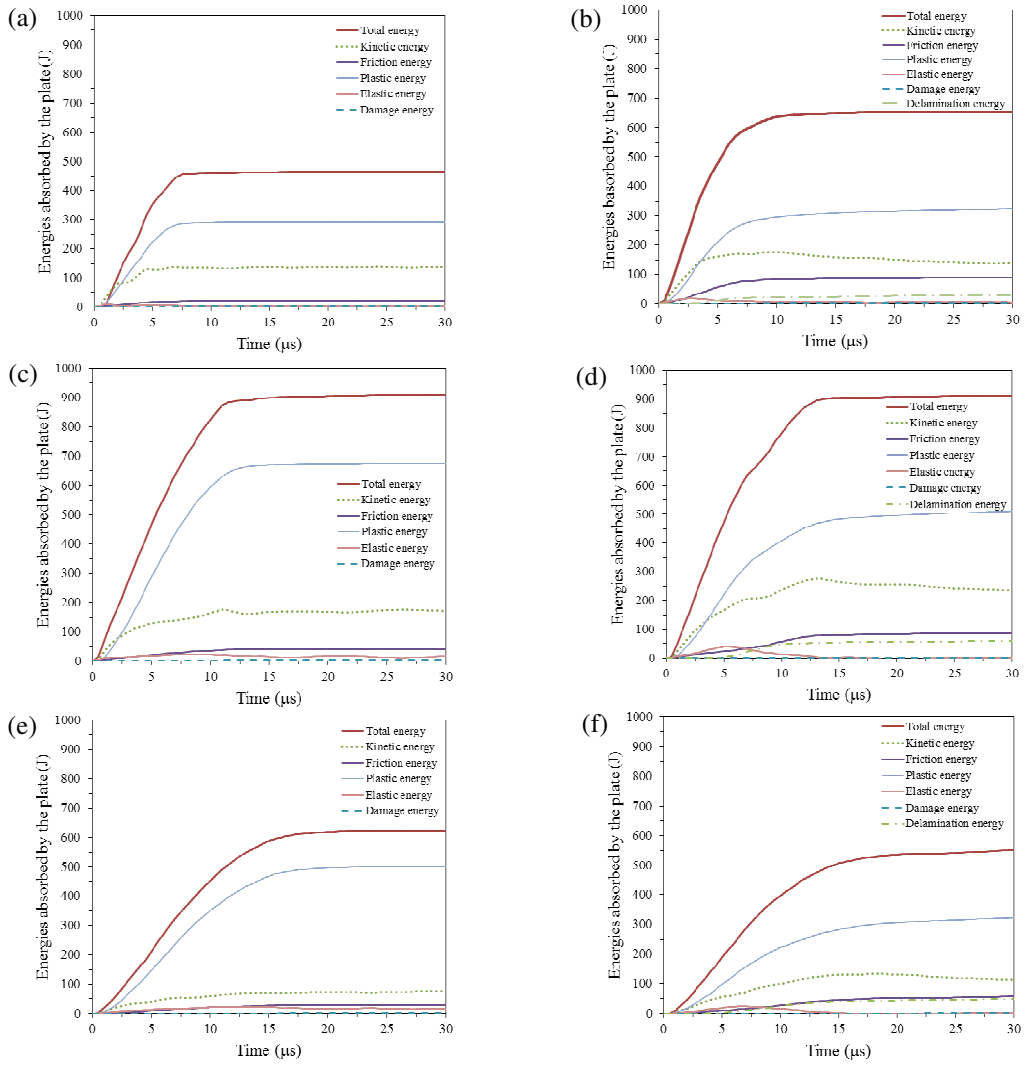

Fig. 9 Components of the energy absorbed by 5.4-mm (a) bulk plate and (b) nacre-like plate impacted at 900 m/s; 9.6-mm (c) bulk plate and (d) nacre-like plate impacted at 900 m/s; and 9.6-mm (e) bulk plate and (f) nacre-like plate impacted at 600 m/s.

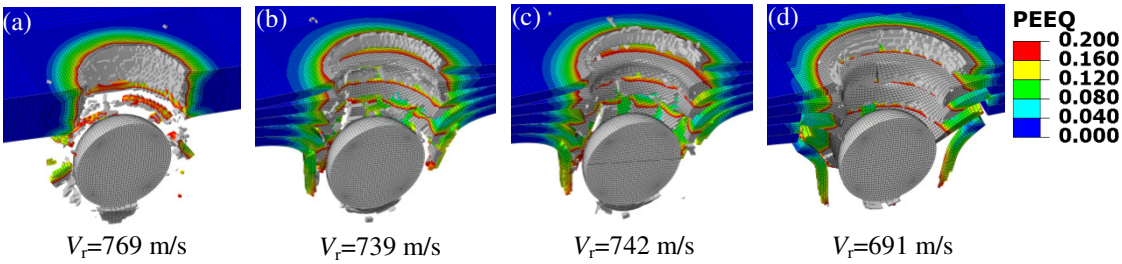

Fig. 10 Comparison of residual velocities V_r and penetration of 5.4-mm plates impacted at 900 m/s: (a) bulk, (b) continuous flat layers, (c) continuous wavy layers and (d) nacre-like plate.

Figures 9(c)-(d) show the components of impact energy absorbed by the 9.6-mm bulk and nacre-like plates, respectively, for an impact velocity of 900 m/s, while Figs. 9(e)-(f) are for bulk and nacre-like plates, respectively, for an impact velocity of 600 m/s.

Although the total energy absorbed by both plates is similar at 900 m/s (Figs. 9(c)-(d)), the contribution of the absorbed plastic dissipation to the total energy absorbed by the plate is larger for the bulk plate, which is more evident for 600 m/s (Figs. 9(e)-(f)). This behaviour

contrasts with the larger plastic dissipation absorbed by the 5.4-mm nacre like plate when compared to the bulk plate of same thickness.

The kinetic energy of the ejected fragments for both bulk and nacre-like plates was estimated by calculating the mass of the fragments and their exit velocity. Loss of mass due to eroded elements was also taken into account to calculate the debris kinetic energy. It was found that kinetic energy of the ejected fragments was up to 14% and 8% of the total energy absorbed by the 5.6-mm thick bulk and nacre-like plates, respectively, when impacted at 900 m/s. The kinetic energy of the ejected fragments in the bulk plate was larger than that of nacre-like plate because of fragmentation and plugging failure observed in the bulk plate.

3.3 Performance of discontinuous layer (nacre-like) plate *vs* continuous layer (bulk, flat, wavy) plates

To demonstrate the advantage of using layers made of tablets instead of layers made of continuous material, numerical models of 5.4-mm thick plate with either continuous flat layers or continuous wavy layers were built. The performance of these configurations for an impact velocity of 900 m/s is shown along with the performance of the bulk plate and nacre-like plate in Fig. 10 by comparing the residual velocity of the projectile V_r and the area of plastic deformation (PEEQ). It is seen that, in this instance, the impact of waviness on the performance of the continuous layer plates is rather marginal. The exercise reveals, however, that there is significant gain to be had through layering, with a 3.4% reduction of the residual velocity for continuous layers, 10.2% reduction for nacre-like plate, and much larger plastically deformed area (Fig. 10) for the layered models as opposed to the bulk plate. The performance of the nacre-like plate was better when compared to that of the continuous layer plates with a 6.5% reduction of the residual velocity and slightly larger area of plastic deformation (Fig. 10(b)-(d)), which indicates that the tablets arrangement allows more diffused plastic deformation.

When designing nacre-like engineering composites, several structural parameters may influence the performance of the structure. Previous research has shown that the waviness [3, 9], aspect ratio and staggered pattern of tablets [32-34], interface properties [3, 9] and the number of hierarchical levels [35] are crucial parameters to take into consideration for the design of these bioinspired structures. Therefore, further work has to be carried out to assess all the aforementioned parameters to obtain an optimal design for aluminium alloy lightweight armour. However, the results presented in this paper using the selected thicknesses are insightful as a starting point for further work in the design of lightweight armour using nacre-like bioinspired composites.

4 SUMMARY AND CONCLUSIONS

A series of numerical analysis were performed to evaluate the ballistic performance of nacre-like AA7075 composite plates against that of bulk aluminium plates. It was found that the composite structures showed significant improvement for 5.4-mm plate thickness, which was explained by the fact that the layering caused a radical change in failure mode for the thin plate, from brittle and localized failure in the bulk plate to more diffuse failure in the layered one.

For the thicker 7.5-mm and 9.6-mm plates however, the improvement brought about by the nacre-like layering was marginal, given that the ductile failure of the bulk plate was already very diffused before perforation. It was also observed that, at lower impact velocities, the composite plates performed worse than the bulk plate especially because of the increase of bending resistance of the bulk plate at low impact velocities. In other words, the performance improvement of the proposed nacre-like AA 7075 composite over the bulk

material is dependent on the plate thickness and projectile velocity.

A comparison of the ballistic performance of 5.4-mm thick plates impacted at 900 m/s for continuous (flat and wavy) layers and discontinuous layers (nacre-like) showed that using tablets resulted in a better performance indicated by lower projectile residual velocity and larger area of plastic deformation.

The study presented in this paper enables us to draw the conclusion that the gain in ballistic performance of nacre-like aluminium composite plates definitely warrants further investigation of these materials for applications in protective structures. However the weight-saving potential needs to be carefully assessed for each specific application, given the sensitivity of the performance to factors such as plate thickness and impact velocity.

ACKNOWLEDGEMENTS

This work was supported in part by the Australian Research Council Centre of Excellence for Design in Light Metals (CE0561574) and the National Natural Science Foundation of China (No. 11232003). Support from the Australian Research Council to Irene Guiamatsia and Giang Nguyen via project DP1093485 is acknowledged.

REFERENCES

[1] Zaera R. Ballistic Impacts on Polymer Matrix Composites, Composite Armor, Personal Armor In: Abrate S, editor. Impact Engineering of Composite Structures, vol. 526: Springer Vienna; 2011. p. 305-403.
[2] Barthelat F. Biomimetics for next generation materials. Philos Trans R Soc A 2007;365(1861):2907-2919.
[3] Espinosa HD, Rim JE, Barthelat F, Buehler MJ. Merger of structure and material in nacre and bone – Perspectives on de novo biomimetic materials. Prog Mater Sci 2009;54(8):1059-1100.
[4] Chen P-Y, McKittrick J, Meyers MA. Biological materials: Functional adaptations and bioinspired designs. Prog Mater Sci 2012;57(8):1492-1704.
[5] Meyers MA, Chen P-Y, Lin AY-M, Seki Y. Biological materials: Structure and mechanical properties. Prog Mater Sci 2008;53(1):1-206.
[6] Hideki K, Taro S. The toughening mechanism of nacre and structural materials inspired by nacre. Sci Technol Adv Mater 2011;12(6):064710.
[7] Sun J, Bhushan B. Hierarchical structure and mechanical properties of nacre: a review. RSC Adv 2012;2(20):7617-7632.
[8] Barthelat F, Zhu D. A novel biomimetic material duplicating the structure and mechanics of natural nacre. J Mater Res 2011;26(10):1203-1215.
[9] Barthelat F, Tang H, Zavattieri PD, Li CM, Espinosa HD. On the mechanics of mother-of-pearl: A key feature in the material hierarchical structure. J Mech Phys Solids 2007;55(2):306-337.
[10] Humburg H, Zhu D, Beznia S, Barthelat F. Bio-inspired tapered fibers for composites with superior toughness. Compos Sci Technol 2012;72(9):1012-1019.
[11] Yao H, Song Z, Xu Z, Gao H. Cracks fail to intensify stress in nacreous composites. Compos Sci Technol 2013;81:24-29.
[12] Knipprath C, Bond IP, Trask RS. Biologically inspired crack delocalization in a high strain-rate environment. J R Soc Interface 2012;9(69):665-676.
[13] Rim JE, Zavattieri P, Juster A, Espinosa HD. Dimensional analysis and parametric studies for designing artificial nacre. J Mech Behav Biomed Mater 2011;4(2):190-211.
[14] Tran P, Ngo T, Mendis P. Bio-inspired composite structure subjected to underwater impulsive loading. In: Salami B, Attard MM, Song C, editors. From Materials to Structures: Advancement through Innovation: CRC Press; 2013. p. 775-780.
[15] Børvik T, Hopperstad OS, Pedersen KO. Quasi-brittle fracture during structural impact of AA7075-T651 aluminium plates. Int J Impact Eng 2010;37(5):537-551.
[16] Brar NS, Joshi VS, Harris BW. Constitutive model constants for Al7075-T651 and Al7075-T6. AIP Conf Proc 2009;1195(1): 945–948.
[17] Dorogoy A, Karp B, Rittel D. A Shear Compression Disk Specimen with Controlled Stress Triaxiality under Quasi-Static Loading. Exp Mech 2011;51(9):1545-1557.
[18] Wang RX, Shayganpur A, Sareskani S, Spelt JK. Analytical Peel Load Prediction as a Function of Adhesive Stress Concentration. J Adhes 2006;82(1):39-61.
[19] Guiamatsia I, Nguyen GD. A thermodynamics-based cohesive model for interface debonding and friction. Int J Solids Struct 2014;51(3-4):647-659.
[20] Abaqus Analysis User's Manual (Version 6.11), SIMULIA.2011.
[21] Johnson GR, Cook WH. A constitutive model and data for metals subjected to large strains, high strain rates and high temperatures. Proceedings of the 7th International Symposium on Ballistics, The Hague, The Netherlands1983. p. 541-547.
[22] Johnson GR, Cook WH. Fracture characteristics of three metals subjected to various strains, strain rates, temperatures and pressures. Eng Fract Mech 1985;21(1):31-48.
[23] Holmen JK, Johnsen J, Jupp S, Hopperstad OS, Børvik T. Effects of heat treatment on the ballistic properties of AA6070 aluminium alloy. Int J Impact Eng 2013;57(0):119-133.
[24] Iqbal MA, Khan SH, Ansari R, Gupta NK. Experimental and numerical studies of double-nosed projectile impact on aluminum plates. Int J Impact Eng 2013;54(0):232-245.
[25] Einav I, Houlsby GT, Nguyen GD. Coupled damage and plasticity models derived from energy and dissipation potentials. Int J Solids Struc 2007;44(7–8):2487-2508.
[26] Børvik T, Forrestal MJ, Hopperstad OS, Warren TL, Langseth M. Perforation of AA5083-H116 aluminium plates with conical-nose steel projectiles - Calculations. Int J Impact Eng 2009;36(3):426-437.
[27] Børvik T, Olovsson L, Dey S, Langseth M. Normal and oblique impact of small arms bullets on AA6082-T4 aluminium protective plates. Int J Impact Eng 2011;38(7):577-589.
[28] Flores-Johnson EA, Saleh M, Edwards L. Ballistic performance of multi-layered metallic plates impacted by a 7.62-mm APM2 projectile. Int J Impact Eng 2011;38(12):1022-1032.
[29] Iqbal MA, Gupta NK. Ballistic Limit of Single and Layered Aluminium Plates. Strain 2011;47:e205-e219.
[30] Dey S, Børvik T, Hopperstad OS, Leinum JR, Langseth M. The effect of target strength on the perforation of steel plates using three different projectile nose shapes. Int J Impact Eng 2004;30(8-9):1005-1038.
[31] Recht RF, Ipson TW. Ballistic perforation dynamics. J Appl Mech 1963;30:384-390.
[32] Ji B, Gao H. Mechanical properties of nanostructure of biological materials. J Mech Phys Solids 2004;52(9):1963-1990.
[33] Lei HJ, Zhang ZQ, Han F, Liu B, Zhang YW, Gao HJ. Elastic Bounds of Bioinspired Nanocomposites. J Appl Mech 2013;80(6):061017-061017.
[34] Zhang ZQ, Liu B, Huang Y, Hwang KC, Gao H. Mechanical properties of unidirectional nanocomposites with non-uniformly or randomly staggered platelet distribution. J Mech Phys Solids 2010;58(10):1646-1660.
[35] Zhang Z, Zhang Y-W, Gao H. On optimal hierarchy of load-bearing biological materials. Proc R Soc B 2011;278(1705):519-525.